J. Fluid Mech. (1992), *vol.* 235, *pp.* 57–72
Printed in Great Britain

Controlled interactions in a forced axisymmetric jet. Part 2. The modulation of broadband turbulence

By R. A. PETERSEN† AND T. A. LONG
Department of Aerospace and Mechanical Engineering, University of Arizona, Tucson, AZ 85721, USA

(Received 6 January 1990 and in revised form 7 July 1991)

Incoherent turbulent motion modulated by coherent large-scale motion contributes to second-order coherent stresses. The spatial distribution of wave-induced stress was measured in a jet whose cross-section had been distorted through controlled resonant interactions between two forced, helical waves spinning in opposite directions. The transfer of energy from the coherent motion to broadband turbulence is documented. Shape assumptions are examined by comparing radial distributions to predictions from linear, inviscid stability theory. Control over small-scale mixing is examined by demodulating the coherent envelope of small-scale turbulence and by correlating it with features of the coherent, large-scale motion. Coherent production is shown to be associated with the roll-up process and there is evidence of secondary, inflexional instabilities.

1. Introduction

The controlled distortion of the cross-section of a jet issuing from a circular nozzle was discussed by Long & Petersen (1992, hereinafter referred to as I). The emphasis was on resonant interactions between forced, spinning waves and on the energy exchange to the mean flow. All of those interactions concerned the large-scale turbulence which contains most of the energy.

Here, in Part 2, the influence of forcing on the broadband turbulence will be emphasized. In particular the ability of the largest scales to organize the smallest scales will be examined. This has direct implications for active control of molecular mixing.

There have been several studies that have demonstrated some degree of control over mixing. Schadow *et al.* (1984) observed improved combustion efficiency using elliptic nozzles of varying aspect ratio. Gutmark *et al.* (1987) demonstrated that square and triangular nozzle shapes also promote enhanced combustion. Moreover, they demonstrated that the combustion was phase locked to the large turbulence scales. Even though the small-scale mixing was incommensurate in frequency with the large-scale motion of the flow it was modulated by the large scales. Mixing can be suppressed as well as enhanced. Roberts (1984) demonstrated that the production of reaction products was suppressed following nonlinear saturation of an excited instability in a plane mixing layer.

Understanding how broadband turbulence is organized by the large-scale motion

† Current address: Jet Propulsion Laboratory, Pasadena, CA 91109, USA.

is essential for turbulence modelling. Many models for turbulent shear flows are based on deterministic analogies to solutions of linearized stability equations. In making comparisons with phase-averaged quantities that are first order in amplitude there is some formal validity to these analogies in that the Rayleigh equation can be derived directly from the linearized, phase-averaged equations of motion (Petersen & Samet 1988).

However, second-order quantities contain contributions from incoherent components of the flow. Consequently a closure scheme is required in order to model those quantities. In a statistical model, Tam & Chen (1979) used eigenmodes calculated from linear stability theory as a set of basis functions. Energy integral methods (reviewed by Liu 1981) use stability eigenfunctions as 'shape assumptions' to model cross-stream distributions of turbulence quantities.

The present study is concerned with the interaction between two spinning waves that were forced acoustically from an array of speakers. The degree to which the inccherent broadband turbulence was organized by the forcing was determined. The relative importance of coherent and incoherent processes to the exchange of energy was examined. The region of the flow where the time-averaged Reynolds stress can be correctly modelled by coherent terms was determined. Small-scale turbulence was demodulated from the organized, large-scale motion and some mechanisms for the control over mixing were explored.

2. Wave-induced stresses

Following Hussain & Reynolds (1970) the velocity field can be decomposed into a time-averaged component, and a phase-incoherent component:

$$u_i(\boldsymbol{x},t) = U_i(\boldsymbol{x}) + \hat{u}_i(\boldsymbol{x},t) + u_i'(\boldsymbol{x},t). \tag{2.1}$$

The time-averaged $U_i = \bar{u}_i$, the phase-coherent component $\hat{u}_i = \langle u_i \rangle - U_i$, and the phase-incoherent component $u_i' = u_i - \langle u_i \rangle$. Each component independently satisfies continuity. Also the time averages of $\hat{u}_i$ and u_i' are both zero. The experimental technique for measuring phase-averaged quantities such as $\langle u_i \rangle$ is described in I.

The phase-averaged covariance is

$$\langle (u_i - U_i)(u_j - U_j) \rangle = \hat{u}_i \hat{u}_j + \langle u_i' u_j' \rangle. \tag{2.2}$$

The time average of (2.2) is equal to the Reynolds stress.

Second-order interactions between coherent disturbances are responsible for the term $\hat{u}_i \hat{u}_j$. The superposition of two helical waves spinning in opposite directions results in a standing wave pattern:

$$\begin{aligned} \hat{u}_i &= \tfrac{1}{2} F_i(x,r)\, \mathrm{e}^{\mathrm{i}(\alpha x + m\phi - 2\pi t/T)} + \tfrac{1}{2} F_i(x,r)\, \mathrm{e}^{\mathrm{i}(\alpha x - m\phi - 2\pi t/T)} + \text{c.c.} \\ &= 2|F_i(x,r)| \cos(m\phi) \cos(\alpha x - 2\pi t/T + \psi), \end{aligned} \tag{2.3}$$

where $|F_i|$ and ψ are the modulus and phase of the radial eigenfunction $F_i(x,r)$. The product $\hat{u}_i \hat{u}_j$ is

$$\begin{aligned} \hat{u}_i \hat{u}_j = |F_i|\,|F_j| + |F_i|\,|F_j| \cos(2m\phi) \\ + |F_i|\,|F_j| [1 + \cos(2m\phi)] \cos[2(\alpha x - 2\pi t/T + \psi)]. \end{aligned} \tag{2.4}$$

The time average of (2.4) is the wave stress. The wave stress contributes to the

development of the mean flow through the Reynolds-averaged momentum equation. The first term on the right-hand side of the equation is uniform in ϕ. It contributes to the mean spreading of the mixing layer. The second term is periodic in ϕ. It contributes to the distortion of the jet cross-section as described in I. The third term is periodic in time and so it vanishes when time averaged.

The incoherent motion organized by the forcing is included in the term $\langle u_i' u_j' \rangle$, which in general can be decomposed into the superposition of a steady term uniform in ϕ, a steady term periodic in ϕ, plus a term periodic in time with zero mean:

$$\langle u_i' u_j' \rangle = [\overline{u_i' u_j'}]_1 (x, r) + [\overline{u_i' u_j'}]_2 (x, r, \phi) + \hat{r}_{ij}(x, r, \phi, t). \tag{2.5}$$

In the absence of forcing the second and third terms on the right-hand side of (2.5) should vanish because of spatial and temporal homogeneity. In the presence of forcing their existence is largely the result of phase and amplitude jitter of the large scales as well as modulation of small-scale turbulence.

The term $[\overline{u_i' u_j'}]_2 (x, r, \phi)$ is a wave-induced stress that contributes, along with $|F_i| |F_j| \cos(2m\phi)$ from (2.4), to the distortion of the jet cross-section. The term $\hat{r}_{ij}(x, r, \phi, t)$ is defined to have zero time average. It is important to the transfer of energy from the coherent, large-scale motion to the incoherent turbulence. Statistically the transfer is represented in the energy budget by the term $\overline{\hat{r}_{ij} \partial \hat{u}_i / \partial x_j}$ (Reynolds & Hussain 1972, equation 3.2).

The various deterministic techniques for modelling wave stresses and wave-induced stresses all involve some kind of an *ad hoc* closure scheme for modelling $\hat{r}_{ij}$. Models based on nonlinear stability theory derive amplitude equations by retaining higher-order terms in a perturbation expansion (e.g. Wygnanski, Marasli & Champagne 1987). These models are based on a quasi-laminar closure scheme in which the $\hat{r}_{ij}$ are set to zero. The energy integral approach is an alternative to the weakly nonlinear formalism (e.g. Liu 1981). Energy integral theories are generally based on closure schemes in which the $\hat{r}_{ij}$ are expressed in terms of the wave strain rate. Shape assumptions, which are usually based on solutions to stability equations, are required in order to model cross-stream distributions.

The important components of $\hat{r}_{ij}$ are off-diagonal and cannot be measured with single-wire probes. The drain of energy to the background turbulence caused by $\overline{\hat{r}_{ij} \partial \hat{u}_i / \partial x_j}$ can be assessed by comparing the relative magnitudes of wave stresses and wave-induced stresses. We will identify regions of the flow where the coherent component is dominant and we will determine the quantitative validity of the shape assumption in those regions.

The Reynolds-averaged stress tensor τ_{ij} is defined as

$$\tau_{ij} = \rho[\overline{\hat{u}_i \hat{u}_j} + \overline{u_i' u_j'}]. \tag{2.6}$$

It leads to the streamwise development of the mean flow through the Reynolds-averaged momentum equation. In cylindrical coordinates the streamwise component of the Reynolds-averaged momentum equation can be written

$$\rho \frac{\partial}{\partial x} \frac{U^2}{2} + \rho V \frac{\partial U}{\partial r} = -\frac{1}{r} \frac{\partial (r \tau_{xr})}{\partial r} - \frac{1}{r} \frac{\partial \tau_{x\phi}}{\partial \phi} - \frac{\partial \tau_{xx}}{\partial x}. \tag{2.7}$$

The only component of the Reynolds stress (2.6) that can be measured directly with the array of single-wire probes is τ_{xx}.

The streamwise evolution of τ_{xx} is compared to the evolution of the jet mean cross-

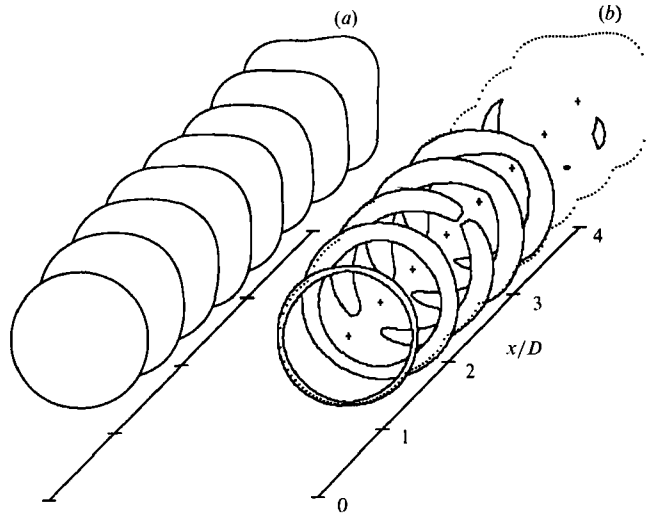

FIGURE 1. Evolution of jet cross-sections from a circular to a square shape. Streamwise locations equally spaced at half-diameter intervals starting with $x/D = 0.5$. Forcing at 206 Hz with spinning mode number combination $m = +2, -2$. (*a*) Mean velocity contour level: $0.5U_j$. (*b*) Turbulence contour level: $(\hat{u}+u')_{rms} = 0.12U_j$.

section in figure 1. The measurement locations were equally spaced 0.5 diameters apart in the streamwise direction beginning at $x/D = 0.5$. The jet was forced simultaneously with spinning mode numbers of $m = +2$ and $m = -2$, which produced a square, $\cos(4\phi)$, cross-section. The turbulence-level contour was selected arbitrarily at 0.12; that rather high level emphasizes the region of the flow between $x/D = 0.5$ and 2.5 where the turbulence was most intense. That region coincided with the evolution of the jet cross-section from a circular to a square shape. At $x/D = 0.5$ the maximum turbulence levels occurred at the polar locations that would evolve into the corners of the square. At $x/D = 1.0$ and beyond, the local maxima shifted to polar locations that were evolving into the sides of the square cross-section. Beyond $x/D = 2.5$ the jet retained its square shape and the turbulence levels fell below the contour threshold. When the jet was forced with spinning mode numbers of $m = +1$ and $m = -1$ the cross-section evolved into an elliptic, $\cos(2\phi)$, shape. Initially, the turbulence levels were largest along the axis that evolved into the major axis of the ellipse. Farther downstream as the elliptical cross-section evolved they were largest along the minor axis.

The wave stress $\overline{\hat{u}^2}$ is compared to the combined stress $\overline{\hat{u}^2}+\overline{\hat{u}'^2}$ in figure 2. Cross-sections 2, 3, and 4 from figure 1 (*b*) are shown. The jet cross-section evolved from a circle to a square over this range. The edges of the mixing layer ($U = 0.3U_j, 0.9U_j$) are shown as dotted contours for reference. The stresses were modulated in polar angle and the highest levels occurred at the sides of the square. The polar angle of the peak level is indicated in each case. The peak r.m.s. turbulence levels in the three cross-sections were 0.17, 0.18, and 0.16 respectively. At $x/D = 0.5$ (not shown) the peak r.m.s. turbulence level was 0.26 and the coherent component accounted for 95% of that value. As the cross-section distortion developed, the coherent fraction of the stress diminished and by $x/D = 2.0$ it accounted for only 52% of the peak r.m.s. value. In terms of mean-square fractions, appropriate for stress ratios, these figures are 90% and 26%, respectively.

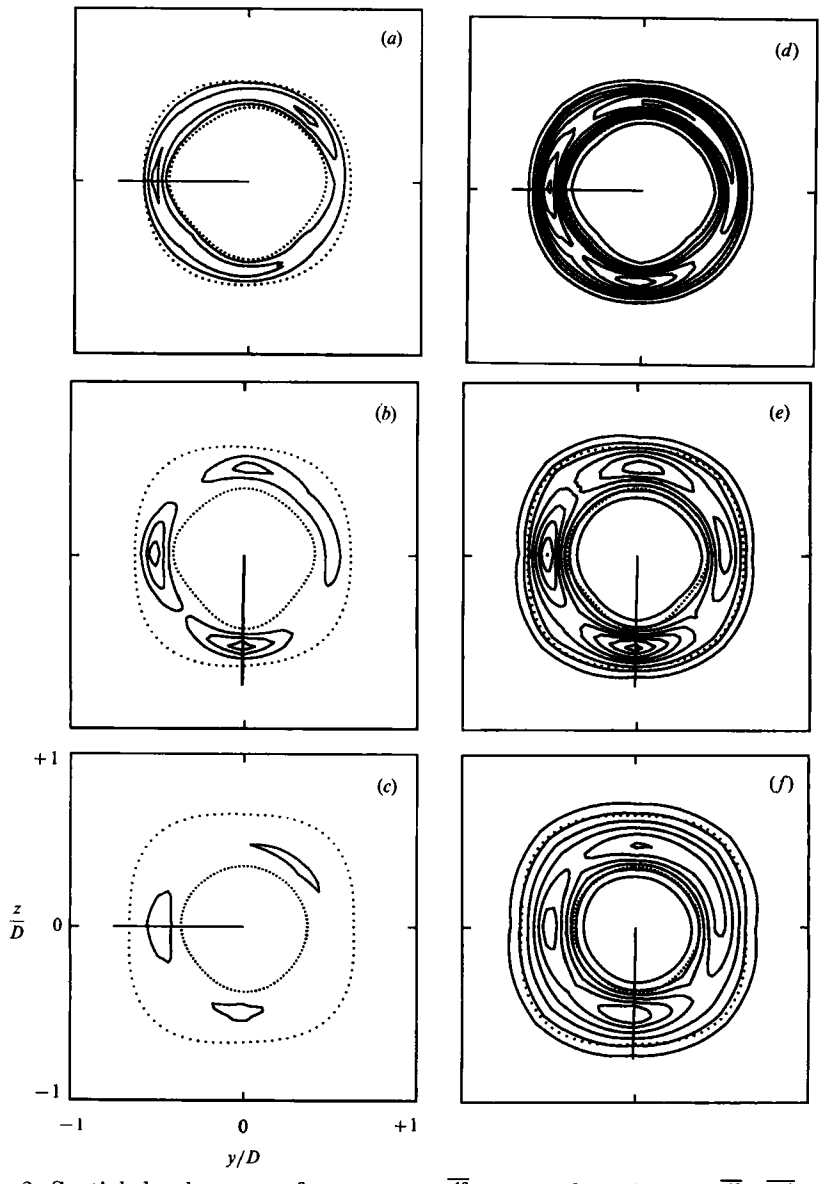

FIGURE 2. Spatial development of wave stress $\overline{\hat{u}^2}$ (*a–c*) and total stress $\overline{\hat{u}^2}+\overline{u'^2}$ (*d–f*). Contour interval: $0.0036U_j^2$. Forcing with spinning mode numbers $m = +2, -2$. Measurement location x/D: (*a, d*) 1.0; (*b, e*) 1.5; (*c, f*) 2.0.

The shape assumption is examined in figures 3 and 4. Radial profiles of wave-induced Reynolds stresses are compared to coherent wave stresses and to eigenfunctions calculated from the Rayleigh stability equations. Fourier decomposition was used to extract the Reynolds stress component that was modulated according to $\cos(2m\phi)$. The radial profile shown in figures 3 and 4 is the Fourier coefficient $c_{2m}(r)$:

$$c_{2m} = (a_{2m}^2 + b_{2m}^2)^{\frac{1}{2}} \tag{2.8}$$

and

$$\begin{bmatrix} a_{2m}(r) \\ b_{2m}(r) \end{bmatrix} = \frac{1}{\pi\rho}\int_0^{2\pi} \tau_{xx}(r,\phi) \begin{bmatrix} \cos(2m\phi) \\ \sin(2m\phi) \end{bmatrix} \mathrm{d}\phi. \tag{2.9}$$

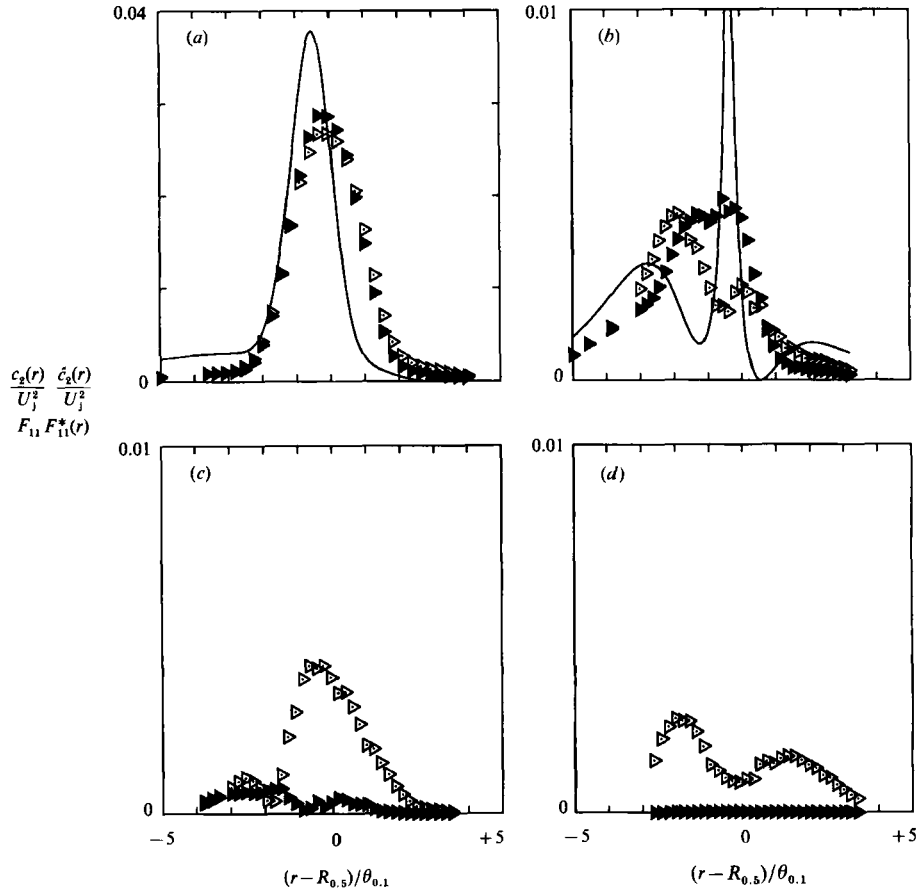

FIGURE 3. Radial profiles of wave stress and wave-induced stress. Forcing with spinning mode numbers $m = +1, -1$. ▷, c_2/U_j^2, equation (2.8); ▶, $\hat{c}_2/U_j^2$; ——, stability eigenfunction, $F_{11}F_{11}^*$. x/D: (*a*) 0.5, (*b*) 1.0, (*c*) 2.0, (*d*) 4.0.

Note that the coefficient c_0 includes the term $[\overline{u'^2}]_1$ in (2.5). The remaining Fourier coefficients include the decomposition of the residual ϕ-dependence of the $[\overline{u'^2}]_2$ term in (2.5).

The wave stress $\overline{\hat{u}^2}$ was decomposed in the same manner. Based on the model equation (2.4) the $\hat{c}_{2m}$ term calculated from $\overline{\hat{u}^2}$ should equal the square of the modulus of the radial eigenfunction. In figures 3 and 4 radial profiles of $\hat{c}_{2m}$ are compared to c_{2m} profiles and to $F_{m1}F_{m1}^*$ profiles calculated from inviscid stability theory. The Rayleigh eigenfunction F_{m1} calculations were based on measured, mean velocity profiles. They were scaled so that the areas under the profiles matched those of the corresponding wave stress profiles. Computational details are described in Petersen & Samet (1988).

At $x/D = 0.5$ (figures 3*a*, 4*a*) the measured profiles were nearly identical. The polar modulation of τ_{xx} was dominated by the wave stress component and the shape assumption, based on the eigenfunction $F_{11}F_{11}^*$, was reasonably accurate. This is a significant finding because τ_{xx} was largest at this point and presumably the momentum transfer to the mean was strongest. By $x/D = 1.0$ (figures 3*b*, 4*b*) the profile based

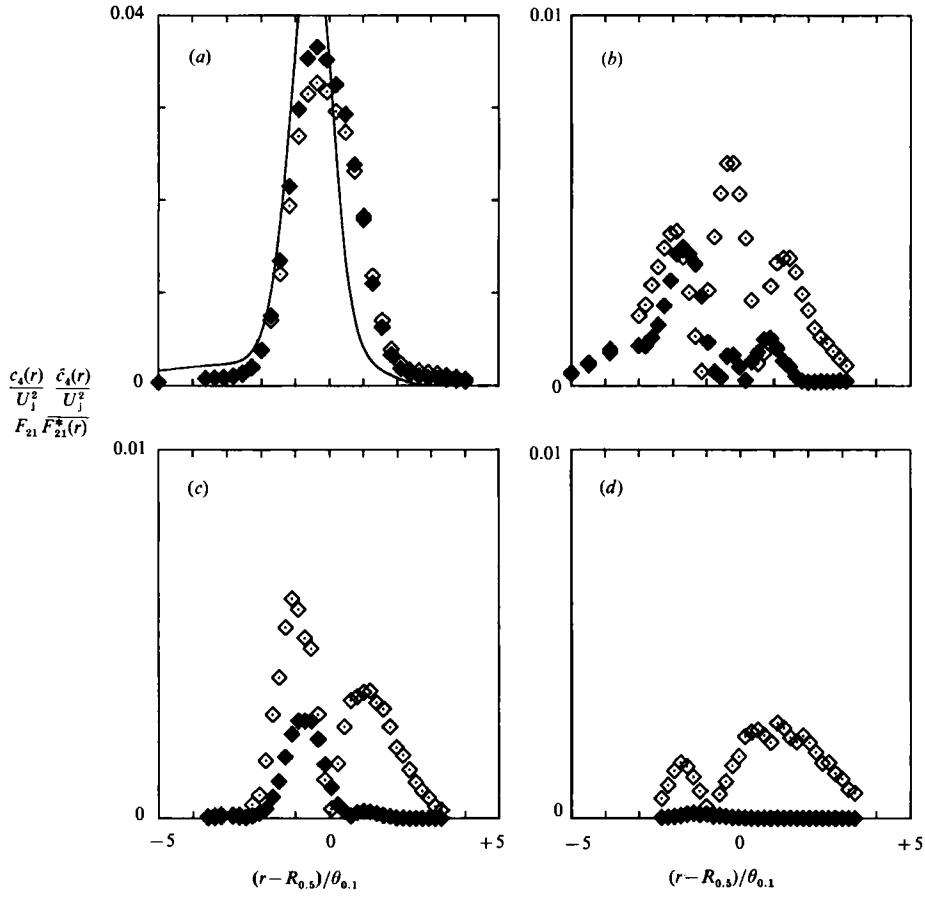

FIGURE 4. Radial profiles of wave stress and wave-induced stress. Forcing with spinning mode numbers $m = +2, -2$. ◇, c_4/U_j^2, equation (2.8); ◆, $\hat{c}_4/U_j^2$; ——, stability eigenfunction, $F_{21}F_{21}^*$. x/D: (*a*) 0.5, (*b*) 1.0, (*c*) 2.0, (*d*) 4.0.

on τ_{xx} was somewhat different from the profile based on wave stress and the shape assumption based on stability eigenfunctions was not very satisfactory.

Streamwise trends are presented in figure 5. Figure 5(*a*) represents the fraction of τ_{xx} modulated according to $\cos(2m\phi)$. The stresses were Fourier decomposed and integrated over the jet cross-section. The area integral of coefficient c_{2m} was divided by the area integral of τ_{xx}. At $x/D = 0.5$, 70% to 80% of the stress was modulated according to $\cos(2m\phi)$. Beyond $x/D = 1.0$ the fraction fell to around 20% and remained at about that level.

Figure 5(*b*) represents the fraction of the modulated stress consisting of wave stress. The remainder represents incoherent background turbulence modulated by the forced wave interaction. The fraction was computed by dividing the area integral of $\hat{c}_{2m}$ by the area integral of c_{2m}. The fraction was largest within the first diameter downstream from the nozzle exit. This distance roughly corresponds to one wavelength of the forced disturbance. Fractions above 100% are not unphysical. This behaviour implies that background turbulence modulated according to $\cos(2m\phi)$ was displaced in ϕ from the wave stresses and so there was some cancellation. Beyond $x/D = 1.0$ the fraction decreased monotonically with streamwise distance.

Based on figure 5 the fraction of turbulence that was modulated according to $\cos(2m\phi)$

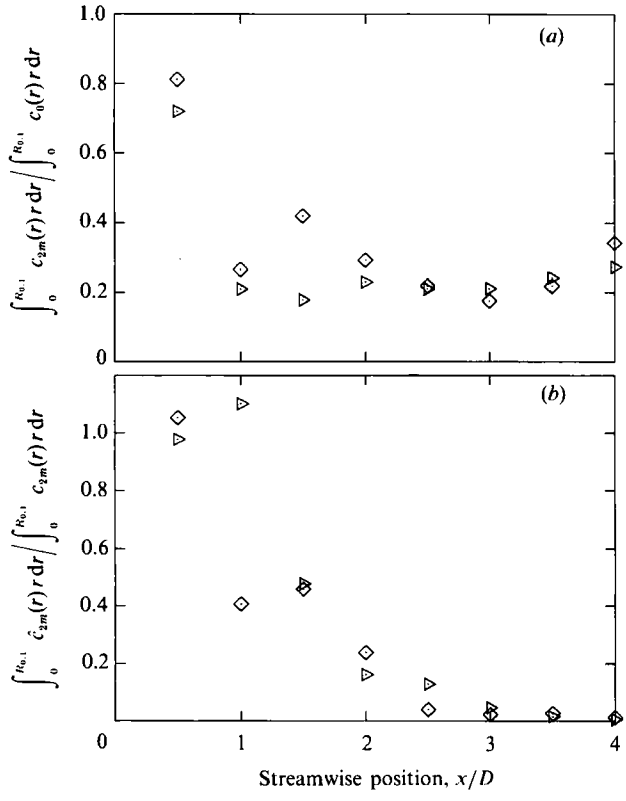

FIGURE 5. Streamwise distribution of (*a*) the fraction of stress τ_{xx} modulated by $\cos(2m\phi)$ and (*b*) the fraction of the modulated stress contained in the coherent, wave stress component. Spinning mode number combination: ▷, $' = +1, -1$; ◇, $m = +2, -2$.

remained nearly constant beyond $x/D = 1.0$. However, there was a continuous drain of energy away from the coherent motion to the organized, background turbulence. This trend may be the cumulative effect of phase and amplitude jitter.

3. Small-scale turbulence

In this section the control over molecular mixing is considered. Incoherent, small-scale turbulence is modulated to some extent by the forced, large-scale motion. The approach here is to demodulate the phase-coherent envelope and to correlate it with features of the large-scale coherent structures.

The signal processing technique illustrated in figure 6 was used to demodulate the envelope $\langle u'^2 \rangle_{ss}$ of small-scale turbulence from the broadband background. The velocity signal was prefiltered using a high-pass, digital filter. The filtered signal was squared and then phase averaged. When the velocity signal was prefiltered at the frequency of forcing (figure 6*a*) the standard deviation $\sigma'(t) = \langle u'^2(t) \rangle^{\frac{1}{2}}$ contained contributions from jitter in the large scales as well as contributions from the small scales. The peak value of $\sigma'(t)$ was only slightly higher than the uniform background level and was less than the peak value of the phase-averaged velocity $\hat{u}(t)$. When the prefiltering frequency was 3 octaves higher than the frequency of forcing (figure 6*b*) then the standard deviation $\sigma'(t)$ defined the envelope of small-scale fluctuations that were modulated by the large scales. The particular value of the prefiltering

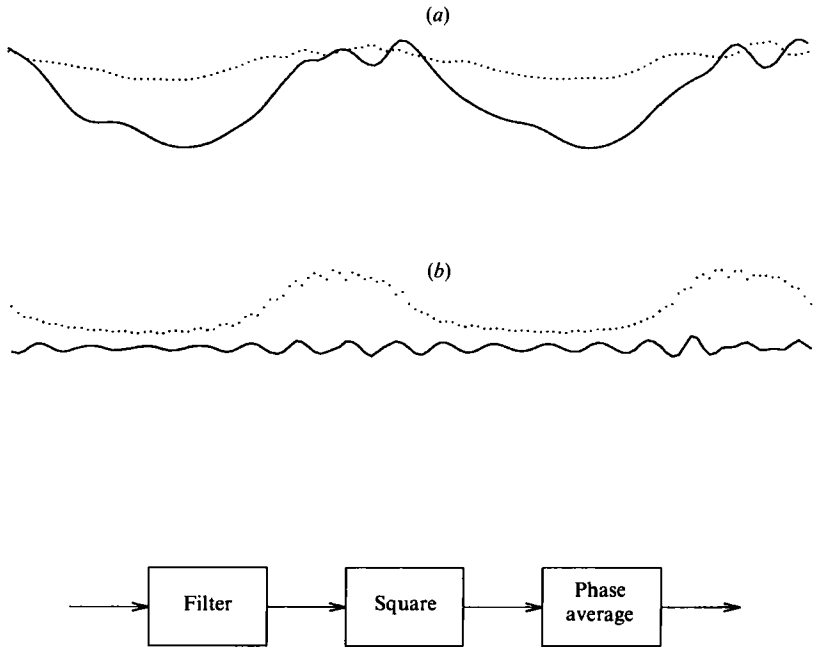

FIGURE 6. Signal processing technique used to demodulate the envelope $\langle u'^2 \rangle_{ss}$ of small-scale turbulence from the broadband spectrum. ——, Prefiltered $\hat{u}(t)$; ...., prefiltered standard deviation $\sigma'(t) = \langle u'^2(t) \rangle^{\frac{1}{2}}$. Forcing frequency was 206 Hz. Low frequency cutoff: (*a*) 206 Hz; (*b*) 1648 Hz.

frequency was arbitrary; the only requirement was that it be above the frequency of the integral scale throughout the measurement region. The peak value of σ' was now considerably higher than both the uniform background level and the prefiltered $\hat{u}(t)$. Figures 6(*a*) and 6(*b*) were each normalized by their respective maxima. The envelope of figure 6(*a*) was dominated by large-scale, energy-containing turbulence. Because the signal shown in figure 6(*b*) was prefiltered well above the frequency of the integral scale the levels were quite low. The random oscillations in $\hat{u}(t)$ apparent in figure 6(*b*) are not visible in figure 6(*a*) because of scaling and are at the level of statistical uncertainty.

Spatial distributions of the envelope of small-scale turbulence $\langle u'^2 \rangle_{ss}$ are shown in figure 7. Because the prefiltering frequency was selected arbitrarily the magnitude of $\langle u'^2 \rangle_{ss}$ is not emphasized here. Instead we emphasize the spatial and temporal distribution. Cuts through the jet cross-section and along a diameter show that turbulent mixing was organized both in space and in time by the forced disturbances. The jet was forced with spinning mode numbers of $m = +2$ and -2, and at a slightly higher level than used with figures 1–5. Cross-sections at $x/D = 2$ show the square, $\cos(4\phi)$, shape of the mean velocity contours (figure 7*a*) and show small-scale turbulence concentrated at the corners of the square (figure 7*b*). Figure 7(*c*) shows a cut through the diameter indicated in figure 7(*b*). The concentration of small-scale turbulence was periodic at the frequency of forcing. Figure 7(*d*) is reprinted from Gutmark *et al.* (1987). It shows combustion products (OH radicals from propane/air using laser-induced fluorescence) in the cross-section of a jet issuing from a square nozzle. The mixing and combustion were enhanced as a result of the interaction between axisymmetric excitation and the square nozzle shape. The reaction zones were localized in space and exhibit a striking resemblance to the present contours of small-scale turbulence (figure 7*b*).

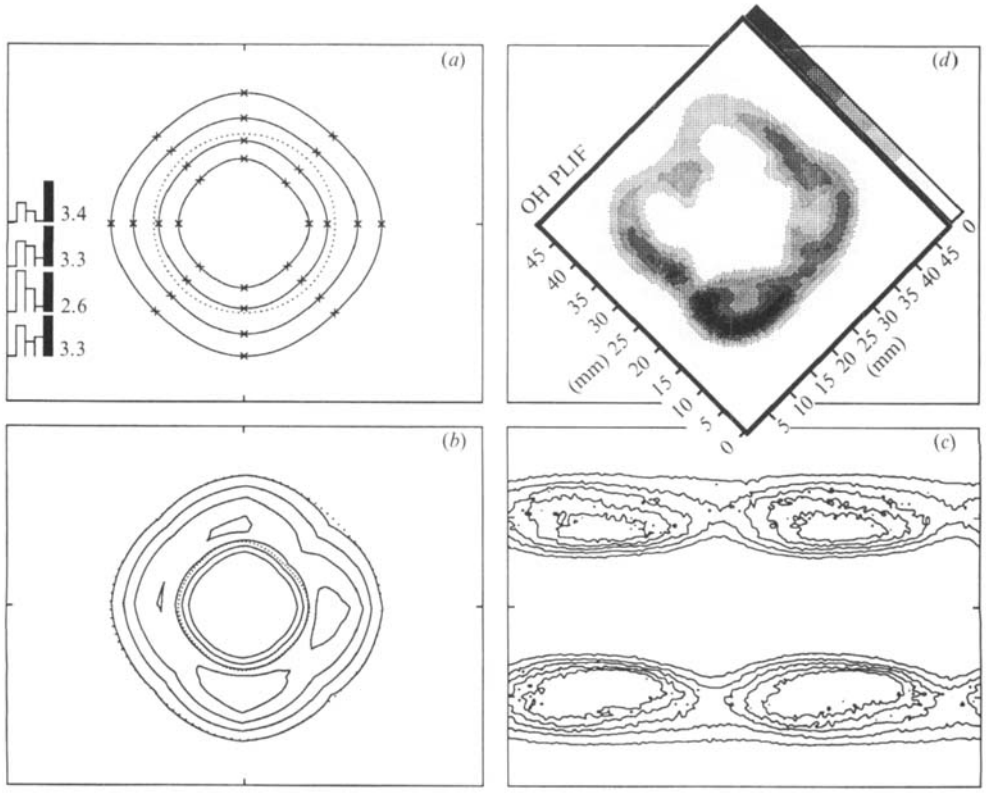

FIGURE 7. Spatial and temporal distributions of small-scale $\langle u'^2 \rangle_{ss}$. Forcing with spinning mode numbers $m = +2, -2$, and measurements at $x/D = 2.0$. (*a*) Mean velocity contours in jet cross-section; contour interval $0.2U_j$ starting at $0.3U_j$. (For an explanation of the spectra on the left see I, the text description of figures 1 and 2.) (*b*) Contours of $\overline{\langle u'^2 \rangle_{ss}}$ in jet cross-section; maximum r.m.s. level $0.034U_j$. (*c*) Contours of $\langle u'^2(t) \rangle_{ss}$ in a cut along the jet diameter; two forcing periods are shown. (*d*) Figure 14(*c*) from Gutmark *et al.* (1987).

In the remaining part of this section we will try to associate the envelope of small-scale turbulence with the spatial structure of the large scales. The feature of the coherent large-scale motion that will be emphasized is phase-averaged vorticity. Vorticity is the field quantity that is most closely linked to what is seen in dye and streakline flow visualizations. It is possible to reconstruct $\langle \omega_\phi \rangle$, the polar component of phase-averaged vorticity, from single-wire data because of the symmetry and spatial filtering inherent in phase-averaged measurements. Based on continuity and assuming a two-dimensional flow, $\langle \omega_\phi \rangle$ can be determined from the following equation:

$$\langle \omega_\phi \rangle = -\frac{\partial}{\partial r}\langle u \rangle - \frac{1}{r}\int_0^r r' \frac{\partial^2}{\partial x^2}\langle u \rangle \, \mathrm{d}r'. \tag{3.1}$$

The continuity assumption, $\partial \langle w \rangle / \partial \phi = 0$, ought to be valid where there are lateral symmetries in the forced, standing wave pattern. This occurs at sides and corners in the case of the square cross-section or along major and minor axes in the case of the elliptic cross-section.

The measurement locations were equally spaced at eighth-wavelength intervals in the streamwise direction. The radial profiles were interpolated to produce data equally spaced at $0.02D$ intervals in radius. First and second derivatives were

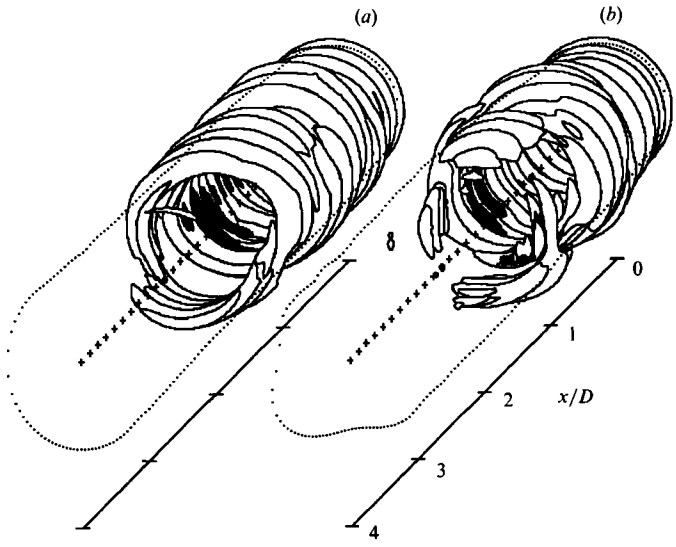

FIGURE 8. Jet sections showing vortex roll-up (contours) and associated $\langle u'^2 \rangle_{ss}$ (darkened regions) at a particular phase of the forcing. Streamwise locations equally spaced at eighth-diameter intervals beginning with $x/D = 0.25$. Vorticity contour level $\langle \omega_\phi \rangle = 2.4 U_j/D$; small-scale turbulence threshold $\langle u'^2 \rangle_{ss}^{\frac{1}{2}} = 0.040 U_j$; mean velocity contour level (dotted contour) $U = 0.5 U_j$. Spinning mode number combination: (*a*) $m = +1, -1$; (*b*) $m = +2, -2$.

calculated numerically using 5-point smoothing. Because of the boundary-layer nature of phase-averaged shear flows the second term in (3.1), which has the greatest potential for error, was generally less than a tenth the size of the first term. The algorithm was tested using 'data' generated analytically from a stream function. Random numbers were superimposed to simulate statistical uncertainty. The analytic vorticity was reconstructed with reasonable accuracy.

Figure 8 is a visualization of the three-dimensional structure of the jet at a specific phase in the forcing. The $m = \pm 1$ and $m = \pm 2$ forcing are shown and the flows are viewed from downstream. The streamwise stations were equally spaced at eighth-diameter intervals beginning at $x/D = 0.25$. At each streamwise station radial distributions of $\langle \omega_\phi \rangle$ were calculated according to (3.1) and interpolated to fill in the polar angles. The contour level shown in the figure was selected to emphasize the initial roll-up. Figure 8(*a*) is oriented such that the major axis of the elliptical cross-section is vertical. Figure 8(*b*) is oriented such that the sides of the square cross-section are horizontal and vertical. The outline of the half-velocity contours is indicated in each case for reference. Some qualitative observations about the coherent structure of the flow can be made based on the figure. The large-scale vorticity of the elliptical jet, forced with spinning mode numbers of $m = \pm 1$, was roughly antisymmetric about the minor axis. By contrast there was a general lateral symmetry to the structure of the square jet, forced with mode numbers of $m = \pm 2$. In the case of the square jet the large-scale vorticity was stronger along the sides, as opposed to the corners, of the square. This last observation is consistent with the conclusions of Gutmark *et al.* (1987) concerning the breakdown of large-scale motion at corners.

Regions of strong mixing modulated by the coherent motion of the flow are indicated in figure 8 as solid domains. The envelope of small-scale turbulence $\langle u'^2 \rangle_{ss}$ was contoured, filled and superimposed onto the vorticity contours. These regions

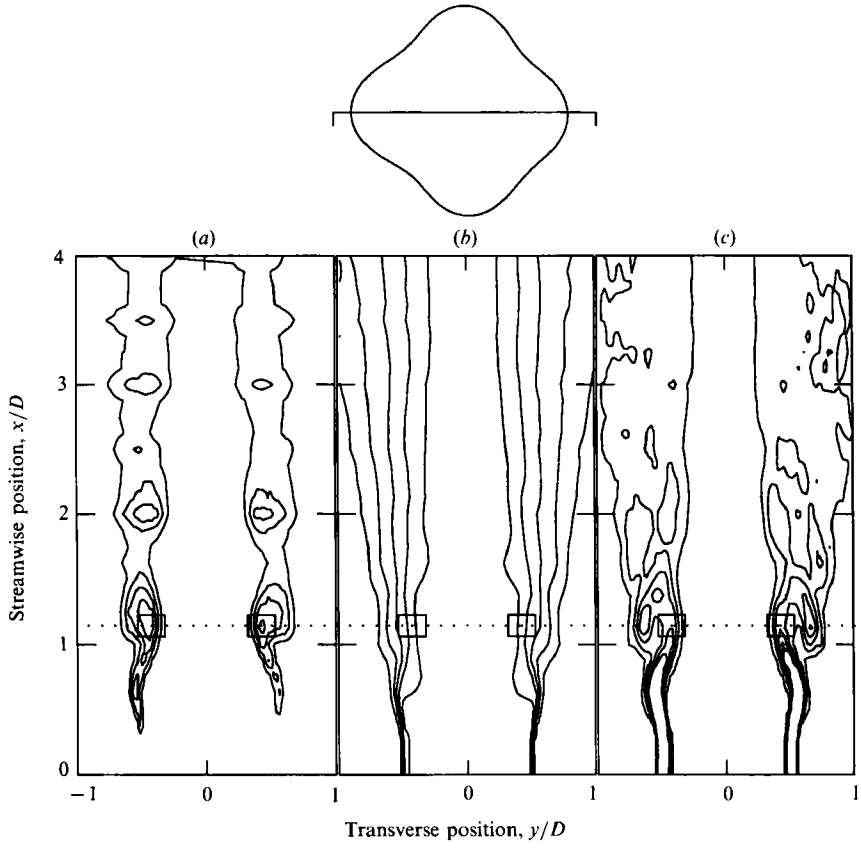

FIGURE 9. Diagonal cut through the corners of the square cross-section at a particular phase of the forcing. Jet was forced with spinning mode numbers $m = +2, -2$. (*a*) Contours of $\langle u'^2(t)\rangle_{ss}$; contour interval: 1000 cm^2/s^2. (*b*) Contours of $\langle u(t)\rangle$; contour interval: 300 cm/s. (*c*) Contours of $\langle \omega_\phi(t)\rangle$; contour interval: 250/s.

are coincident with the region of vortex roll-up. The manner in which they are associated can be understood more precisely by examining the flow structure in planes cut along the jet centreline.

Diagonal and lateral cuts through the corners and sides of the square jet are shown in figures 9 and 10. The phase is identical to that of figure 8(*b*). The spatial distribution of the turbulence envelope $\langle u'^2\rangle_{ss}$ is compared to the simultaneous distributions of phase-averaged velocity $\langle u\rangle$ and vorticity $\langle \omega_\phi\rangle$. The breakdown of large-scale coherent motion at the corners of the square is apparent when figures 9(*c*) and 10(*c*) are compared. Three concentrations of vorticity can be seen in figure 10(*c*) spaced over two wavelengths. In figure 9(*c*) the large-scale vortical structures seem to have disappeared immediately after roll-up. These impressions were confirmed by examining the evolution of the flow at various phases.

The cellular structure evident in figures 9(*a*) and 10(*a*) at the second contour level and at half-diameter intervals in the streamwise direction is an artifact. However, the prominent peaks in the upstream portion of the flow are significant. This was confirmed by tracking their motion at varying phase. The upstream peaks in the envelope of small-scale turbulence occurred in the regions of roll-up. The peaks occurred at the inner edge of the mixing layer and generally at streamwise locations

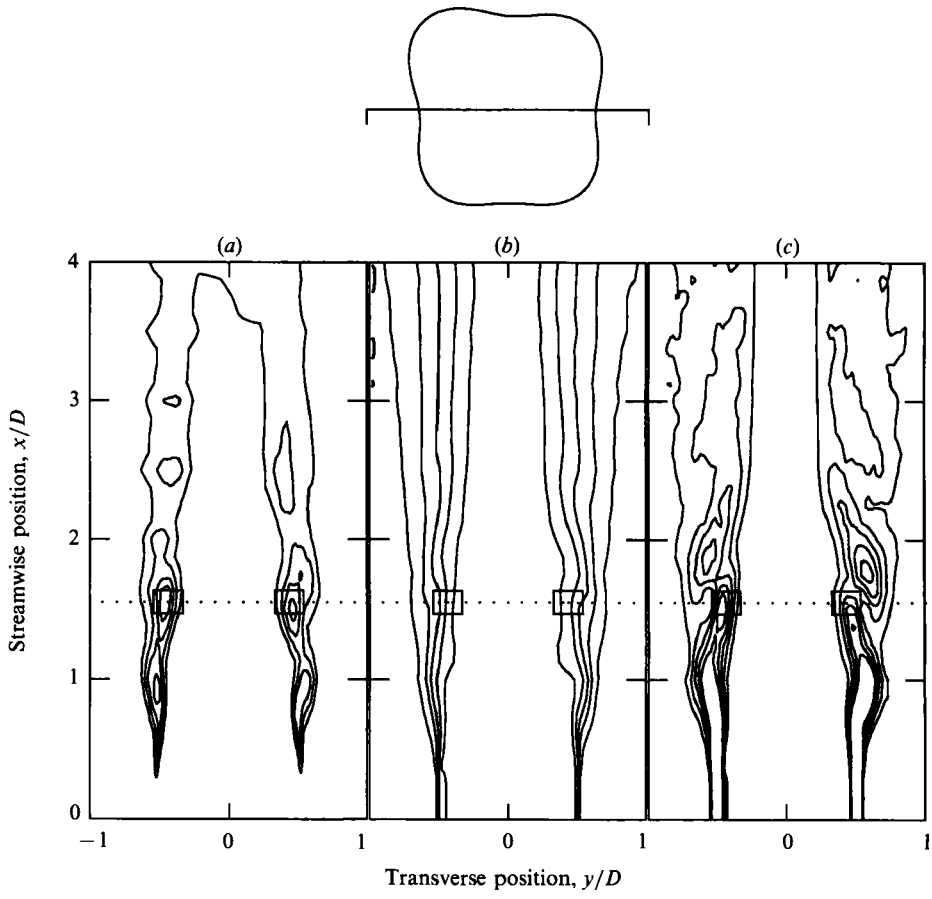

FIGURE 10. Lateral cut through the sides of the square cross-section at a particular phase of the forcing. Conditions identical to figure 9.

where the vorticity exhibited double peaks across the mixing layer in the radial direction. This last finding is significant because multiple maxima in radial profiles of vorticity correspond to multiple inflexion points in radial profiles of velocity. The extra inflexion points create secondary shear layers imbedded inside the primary shear layer which are locally unstable. Local instabilities can lead to local mixing, thus providing a mechanism whereby control of the large scales can indirectly control mixing.

The hypothesis of secondary, inflexional instabilities can be explored further by correlating the phase evolution of transverse profiles of velocity and turbulence. This type of correlation is shown in figure 11. The streamwise station closest to the dotted line of figure 9 was selected. Phases were selected equally spaced over one period of forcing. At each phase the profile of r.m.s. u'_{ss}, magnified by a factor of 10, is superimposed on the corresponding profile of phase-averaged velocity. The phase $t/T = 0.4$ is the same phase as figures 8(*b*) and 9. Time-averaged, small-scale turbulence provides a phase-independent pedestal. Any variation with phase about that pedestal is caused by the forcing. From figure 11 the peak level of u'_{ss} occurred at or immediately before the onset of a multi-inflexional velocity profile. Peak values occurred at the inner edge of the mixing layer. This picture is consistent with

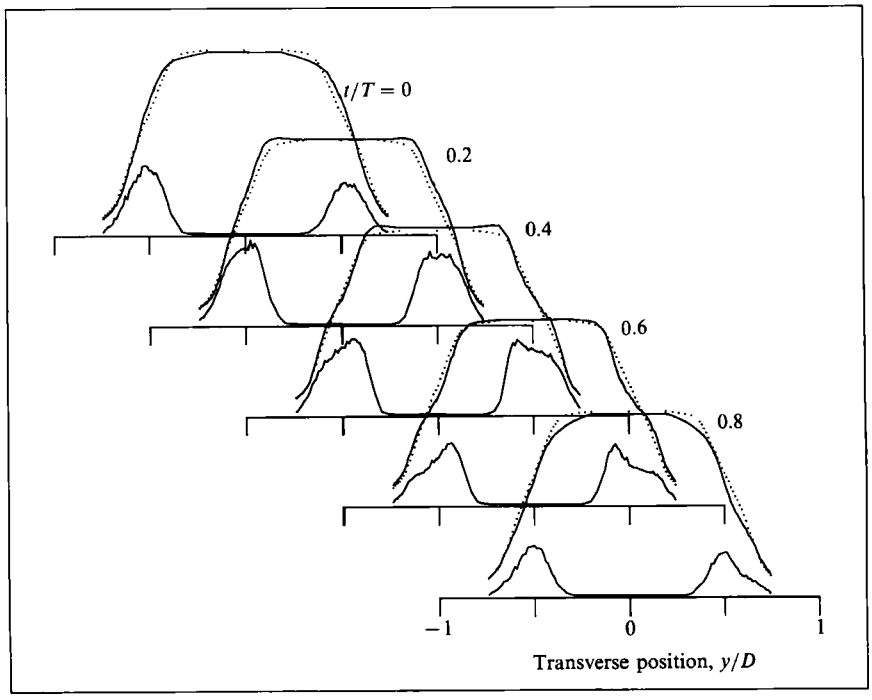

FIGURE 11. Phase evolution of cross-stream distributions of $\langle u(y,t)\rangle$ and $10\langle u'^2(y,t)\rangle^{\frac{1}{2}}_{ss}$ along a diagonal through the corners of the square cross-section at $x/D = 1.125$. ....., Mean velocity profile.

inflexional instabilities that are initiated some point upstream and then develop as they are convected past the point of measurement. This same trend was verified at several other streamwise locations.

4. Conclusions

Incoherent turbulent motion contributes to second-order coherent quantities such as phase-averaged variance, equation (2.2). Components of $\langle u'^2\rangle$ that vary with polar angle ϕ and with the phase of the forcing contribute to wave-induced stress and to energy transfer from the coherent, large-scale motion to the broadband turbulence. Mechanisms by which incoherent, broadband turbulence is modulated by the forcing include phase and amplitude jitter of the forced, large-scale motion and production of small-scale turbulence through secondary instabilities induced by the coherent, large scales. The stress tensor can be obtained from the phase-averaged covariance tensor by averaging over time. Wave-induced stress consists of the coherent wave stress $\overline{\tilde{u}^2}$ plus the component of the incoherent turbulence $\overline{u'^2}$ modulated by the forcing.

The spatial distribution of wave-induced stress was measured in a jet whose cross-section had been distorted through controlled resonant interactions between two forced, spinning waves. In this experiment the forced response of the jet was strongest in the streamwise direction within the first wavelength. Beyond that point, although the ratio of wave-induced stress to total stress remained about constant, there was a continuous shift in energy from coherent motion to incoherent motion organized by the forcing. We speculate that jitter was the likely mechanism for this shift.

Close to the nozzle, where the coherent stresses were very strong, shape assumptions based on eigenfunctions calculated from spatial stability theory accurately modelled the measured stress distributions. One would anticipate that a deterministic model might predict accurately the exchange of momentum from the forced motion to the mean flow in this region. Farther downstream, as the coherent motion lost energy, the agreement with the stability eigenfunctions also deteriorated. Nevertheless deterministic models based on shape assumptions still may give useful qualitative information.

The question of control over molecular mixing was addressed by extracting small-scale turbulence organized by the large-scale, coherent motion. The coherent envelope of small-scale turbulence was demodulated by prefiltering the data prior to measuring the phase-averaged variance. Cuts through a jet cross-section and along a diameter (figure 7) demonstrated that the turbulence was modulated both in space and in phase.

Coherent vorticity $\langle \omega_\phi \rangle$ was estimated by applying continuity and symmetry assumptions to the coherent, streamwise component of velocity. This was done in order to associate the modulation of turbulence with features of the large-scale, coherent motion. When the jet was forced in such a way as to produce a square cross-section the coherent structures at the corners of the square (figure 9), visualized in terms of coherent vorticity, were destroyed. This observation is in agreement with flow visualization of an excited jet issuing from a square nozzle (Gutmark *et al.* 1987).

Small-scale turbulence modulated by the coherent motion was associated with the roll-up process (figures 9 and 10). The turbulence was concentrated at the inner edge of the mixing layer and at streamwise locations where there were multiple inflexion points in the velocity profile. We speculate that the turbulence was produced through secondary, inflexional instabilities. This may explain how molecular mixing might be controlled through the direct control over the large-scale motion of free shear flows.

The authors would like to thank Dr E. Gutmark for supplying us with the original used in figure 7. This research was supported by the National Science Foundation under grant MSM 8800086.

REFERENCES

CHAN, Y. Y. 1977 Wavelike eddies in a turbulent jet. *AIAA J.* **15**, 992–1001.

GUTMARK, E., SCHADOW, K. C., PARR, T. P., PARR, D. M. & WILSON, K. J. 1987 Noncircular jets in combustion systems. *AIAA Paper* 87-1379.

HUSSAIN, A. K. M. F. & REYNOLDS, W. C. 1970 The mechanics of an organized wave in turbulent shear flow. *J. Fluid Mech.* **41**, 241–258.

LIU, J. T. C. 1981 Interactions between large-scale coherent structures and fine-grained turbulence in free shear flows. In *Transition and Turbulence* (ed. R. E. Meyer). Academic.

LONG, T. A. & PETERSEN, R. A. 1992 Controlled interactions in a forced axisymmetric jet. Part 1. The distortion of the mean flow. *J. Fluid Mech.* **235**, 37–55 (referred to herein as I).

PETERSEN, R. A. & SAMET, M. M. 1988 On the preferred mode of jet instability. *J. Fluid Mech.* **194**, 153–173.

REYNOLDS, W. C. & HUSSAIN, A. K. M. F. 1972 The mechanics of an organized wave in turbulent shear flow. Part 3. Theoretical models and comparisons with experiments. *J. Fluid Mech.* **54**, 263–288.

ROBERTS, F. A. 1984 Effects of a periodic disturbance on structure and mixing in turbulent shear layers and wakes. Ph.D. dissertation, California Institute of Technology, Pasadena.

SCHADOW, K. C., WILSON, K. J., LEE, M. J. & GUTMARK, E. 1984 Enhancement of mixing in ducted rockets with elliptic gas-generator nozzles. *AIAA Paper* 84-1260.

TAM, C. K. W. & CHEN, K. C. 1979 A statistical model of turbulence in two-dimensional mixing layers. *J. Fluid Mech.* **92**, 303–326.

WYGNANSKI, I., MARASLI, B. & CHAMPAGNE, F. H. 1987 On the weakly nonlinear stability model applied to a diverging small-deficit wake. *AIAA Paper* 87-1465.